

Formation of Enceladus' Dust Plume —SUPPLEMENTARY INFORMATION

Jürgen Schmidt^{1*}, Nikolai Brilliantov^{1,2}, Frank Spahn¹ & Sascha Kempf³

¹ Universität Potsdam, Nichtlineare Dynamik, D-14469 Germany

² Moscow State University, Russia

³ Max Planck Institut für Kernphysik, Heidelberg, Germany

October 31, 2007

File includes:

Supplementary Methods

Supplementary Notes

Supplementary Equations (S1 to S27)

Supplementary Figures and Legends (S1 to S8)

*Corresponding author. phone: +49 (0)331 977 1626. email: jschmidt@agnld.uni-potsdam.de

The complete model of Enceladus' dust plume has three conceptually different parts: (i) the gas outflow through the channels along with nucleation and growth of icy particles, (ii) grain collisions with channel walls and their interaction with the vapour stream and (iii) formation of the Plume by the ballistic motion of the dust particles. Here, we outline the details and background of the model with the complete set of equations used to simulate the plume.

1 Gasdynamics

To describe the stationary outflow of vapour from the subsurface reservoir to vacuum through channels of variable cross section, we apply a one-dimensional gas-dynamic model for gas streamlines. It uses the following variables: $\rho_{\text{gas}}(z)$, $u_{\text{gas}}(z)$ and $T_{\text{gas}}(z)$, which are, respectively, the density of the gas, its speed and temperature; z is the vertical coordinate along the channel. The nucleation and growth of grains in the gas, naturally, affects the gasdynamics and hence requires additional variables. These are $f(z)$ – the solid fraction and $R(z)$ – the maximal radius of particles at point z , from which the local size distribution can be derived. For a channel with a varying cross-section $S(z)$ the mass conservation affords constant discharge $Q = \rho_{\text{gas}}(z)u_{\text{gas}}(z)S(z)$. The conservation of momentum for the addressed process (gas outflow from the reservoir, kept at the water triple point), is expressed in terms of the Euler gas-dynamic equation [1]. Finally, the energy conservation for a system with a phase transformation (condensation of vapour into ice) is described by the first thermodynamic law. In terms of the introduced variables the conservation equations read

$$\frac{u'_{\text{gas}}}{u_{\text{gas}}} + \frac{\rho'_{\text{gas}}}{\rho_{\text{gas}}} + \frac{S'}{S} = 0 \quad (\text{S1})$$

$$\frac{T'_{\text{gas}}}{T_{\text{gas}}} = -\frac{u_{\text{gas}}u'_{\text{gas}}}{\gamma c_{v,g}T} + f' \left[\frac{H}{\gamma c_{v,g}T_{\text{gas}}} + \frac{\gamma - 1}{\gamma} \right] \quad (\text{S2})$$

$$\frac{\rho'_{\text{gas}}}{\rho_{\text{gas}}} = \frac{1}{\gamma - 1} \left[\frac{T'_{\text{gas}}}{T_{\text{gas}}} - \frac{H}{c_{v,g}T_{\text{gas}}} f' \right] \quad (\text{S3})$$

$$f'(z) = \frac{4\pi\rho_{\text{grain}}}{Q} \int_0^z \gamma_{\text{nuc}}(z_0) [R(z) - R(z_0)]^2 R'(z) S(z_0) \Theta_H(R(z) - R(z_0)) dz_0, \quad (\text{S4})$$

where γ is the adiabatic index ($\gamma = 4/3$ for water), H is the specific sublimation energy,

$$dH/dT = c_{v,g} - c_{\text{ice}}, \quad (\text{S5})$$

with $c_{v,g}$ and c_{ice} being, respectively, the specific heat capacities of water vapour and ice, $\rho_{\text{grain}} = \rho_{\text{ice}}$ is the ice density and $\gamma_{\text{nuc}}(z)$ is the nucleation rate at point z . The Heaviside function is denoted by Θ_H .

The above set of equations is not closed, as additional equations for the particle radius $R(z)$ and nucleation rate $\gamma_{\text{nuc}}(z)$ are needed. These quantities are addressed in the following section.

2 Nucleation and growth of icy grains

2.1 Nucleation rate

An important quantity of the model is the nucleation rate $\gamma_{nuc}(z)$, which gives the number of grains nucleated per unit volume per unit time at a point z in the channel. A number of theories exist for homogeneous nucleation, but none of them is accurate enough, or convenient, for practical application to the current problem. Therefore we use a *direct* fit to experimental data [2] of water nucleation. Namely, we observe that the parameterisation

$$\gamma_{nuc} = B(T_{gas}) (\sigma - 1)^{n(T_{gas})} \quad (S6)$$

gives an excellent description of the experimentally measured dependence of the nucleation rate on the super-saturation (Fig. S1)

$$\sigma = \frac{\rho_{gas}}{\rho_{eq}^{(l.g.)}(T_{gas})}, \quad (S7)$$

defined as the ratio of the gas density ρ_{gas} and its corresponding saturated value, $\rho_{eq}^{(l.g.)}(T_{gas})$. The fitted temperature dependent coefficients read (Fig. S1)

$$\log_{10}[B(T_{gas})] = -32.025880 - 0.070074889 T_{gas} + 0.00040240774 T_{gas}^2 \quad (S8)$$

$$n(T_{gas}) = 1.1743362 + 0.011626596 T_{gas} + 0.00047597152 T_{gas}^2, \quad (S9)$$

In Eq. (S7) we use for $\rho_{eq}^{(l.g.)}(T_{gas})$ the density of the saturated vapour for the liquid-gas equilibrium (see Eq. (S27)). Physically, this reflects the fact that the nuclei of the new phase at these conditions contain only 20-30 water molecules, which is too small to treat them as crystalline.

2.2 Growth rate

Once the grains have nucleated they continue to grow due to interaction with the surrounding gas: Water molecules hit the grains' surface and adsorb on it. The interaction with the gas also determines the dynamics of the grains, namely, their re-acceleration after collisions with the channel walls. For the addressed conditions the mean free path of the water molecules in the gas is at least one order of magnitude larger than the typical size of the grains. Therefore, to describe the vapour-dust interaction, one needs to use gas-kinetic theory. The straightforward calculation of the collision rate of water molecules with the icy grains yields the grains' growth rate

$$\frac{dR}{dz} = \frac{\beta}{\sqrt{2\pi}\gamma \rho_{grain}} \left[\rho_{gas}(z) - \rho_{eq}^{(s.g.)}(T_{gas}(z)) \right] \frac{c_s(z)}{u_{gas}(z)}, \quad (S10)$$

where $c_s(z)$ is the local speed of sound and β is the condensation coefficient [3], giving the fraction of adsorbed molecules, of those which hit the grain. This equation also accounts for a possible evaporation of molecules from the grains surface: If the density of the surrounding vapour $\rho_{gas}(z)$ is

equal to that of the saturated vapour $\rho_{\text{eq}}^{(s.g.)}$ at temperature T_{gas} (we assume that the grains have always the gas temperature T_{gas}) the grains stop to grow. If $\rho_{\text{gas}}(z)$ is smaller than $\rho_{\text{eq}}^{(s.g.)}(T_{\text{gas}})$ the grains start to evaporate. The typical size of the grains, $0.1 - 10 \mu\text{m}$, is large enough to treat them as crystalline, so that the saturated vapour density for the vapour-ice equilibrium, $\rho_{\text{eq}}^{(s.g.)}$, is used (Eq. S26).

Eqs. (S1, S2, S3, S4) together with Eqs. (S6, S7) and (S10) form a complete set, which we solve numerically. In fact, we use modified equations, eliminating ρ'_{gas} and T'_{gas} from (S1, S2, S3) to obtain an equation for u'_{gas} . Then we solve the differential equations for R , f , and u_{gas} with a simple predictor corrector scheme and obtain at each step ρ_{gas} and T_{gas} from the algebraic equations for mass and energy conservation. The numerical difficulty to integrate through the transition to supersonic speeds is surmounted by using the transformation $d\eta = (1 - v^2)dv/v$, where $v = u_{\text{gas}}/c_s$ with the sound speed c_s , and iteration of the starting speed $u_{\text{gas}}(z = 0)$ for a unique solution. The values for density and temperature of the gas change discontinuously from the reservoir to the channel [1] at $z = 0$. The starting values $T_{\text{gas}}(z = 0)$ and $\rho_{\text{gas}}(z = 0)$ are obtained from the temperature and density of the reservoir and $u_{\text{gas}}(z = 0)$ using the adiabatic equation of state and Bernoulli's equation [1].

The above equations are simplified, as we retain (after differentiation) only terms that are zeroth order in f . This is a good approximation, since $f < 0.1$ throughout. Moreover, at this level we assume that the speeds of the grains and gas are the same. Taking into account the difference of these speeds would lead to additional terms on the order of f , which were already neglected in the simplified description. We have checked that the solution to the full (not simplified) equations yields practically indistinguishable results compared to the simplified treatment.

3 Random channels and stochastic wall collisions

3.1 Random channels

To describe the set of cracks which connect a subsurface vapour reservoir with the outer space (vacuum) we adopt the following random channel model. First, we introduce the maximal lateral dimension (i.e. width) of the channels D_{max} and consider channels of a total length L . We fix D_{max} later to be on the order of the collision length L_{coll} , which is constrained by comparing the theoretical results with observations.

Next we assume that the width of the channel depends randomly on the coordinate z along the channel, that is, $D(z)$ is represented by a superposition of sine curves,

$$D(z) = \sum_i A_i \sin(k_i z + 2\pi\xi), \quad (\text{S11})$$

where A_i are the amplitudes of the modes, ξ is a random number uniformly distributed in the interval $[0, 1]$, and the wave numbers are chosen as

$$k_i = \frac{1}{2} \left(\frac{2\pi}{L} \right) i < k_c = \left(\frac{2\pi}{L_0} \right). \quad (\text{S12})$$

Here the subscript i runs over integers $1, 2, 3, \dots$ as long as $k_i < k_c$ is fulfilled. Including the prefactor $1/2$ for the wave number allows for modes with wavelengths twice the total length of the channels. In Eq. (S12) we introduce the cutoff length L_0 , which sets the shortest length for the variation of a channel width (in some sense it quantifies the cracks' irregularity). We associate this length with the correlation length, that characterises correlations between the channel widths $D(z)$ and $D(z')$ at points z and z' and assume an exponentially decaying correlation function

$$\langle D(z)D(z') \rangle - \langle D(z) \rangle^2 \propto \exp \left[-\frac{|z-z'|}{L_0} \right]. \quad (\text{S13})$$

Then the amplitudes of the random modes, consistent with the exponential correlations (S13) read,

$$A_i = \frac{a}{\sqrt{1 + (k_i L_0)^2}}. \quad (\text{S14})$$

From Eqs. (S11, S14) we obtain a random profile, the parameter a being fixed by the narrowest width of the channel D_{\min} . The correlation length L_0 and the reduction of the channel diameter D_{\min}/D_{\max} are the most important quantities which characterise a random channel. Physically, they are determined by the processes of crack formation and evolution and hence may vary over some range.

In practice, to generate a random channel, we choose randomly the correlation length L_0 and the minimal width D_{\min}/D_{\max} uniformly distributed in specified intervals. Using then Eqs. (S11, S12, S14) we find the coefficient a in Eq. (S14), corresponding to the random set $L_0, D_{\min}/D_{\max}$ and ξ . Finally, with the so obtained value a , Eqs. (S11, S12, S14) yield a random channel. In Fig. S2 three different examples of random channels with different pairs of D_{\min}/D_{\max} and L_0 are shown, together with the solutions for the gas density, velocity, nucleation rate, super-saturation, and particle size distribution. The peak size of the grains may vary from submicron up to tens of microns in size, depending on the parameters of the channel.

3.2 Particle size distribution

According to the results of our simulations the nucleation of icy grains and their subsequent growth only take place in a very limited zone, namely, near the nozzle throat $D(z) = D_{\min}$ (Fig. S2). In this zone the size distribution of the grains is for all practical purposes set, and remains almost unaltered up to the outlet. The velocity distribution of particles, which leave a channel, is determined by wall collisions in the outlet region. Hence, the size distribution near the outlet is of the main interest. Let the subscript “ ∞ ” labels quantities at the outlet of the channel. From Eq. (S10) we find the size r of a particle at the outlet that nucleated at location z_0 in the channel

$$r(z_0) = R_\infty - R(z_0). \quad (\text{S15})$$

The concentration of such particles at the point of their origin, $n(z_0)$, may be found from the conservation law,

$$\gamma_{\text{nuc}}(z_0)S(z_0)dz_0dt = n(z_0)u_{\text{gas}}(z_0)S(z_0)dt, \quad (\text{S16})$$

where the left-hand side of this equation gives the amount of particles nucleated during the infinitesimal time interval dt in an infinitesimal volume $S(z_0)dz_0$, while the right-hand side equals the same amount (in a steady-state) removed from this volume by the gas flow. Correspondingly, the concentration of these particles at the outlet, $n(\infty, z_0)$, obeys the continuity equation:

$$n(\infty, z_0)u_\infty S_\infty = n(z_0)u_{\text{gas}}(z_0)S(z_0), \quad (\text{S17})$$

where S_∞ is the cross-section near the outlet. Combining Eqs. (S16) and (S17), taking into account that $n(\infty, z_0)$ gives concentration of particles of size $r(z_0)$ and using $z_0(r)$ – the inverse function to $r(z_0)$, we obtain the size distribution

$$P(r)dr = \frac{\gamma_{\text{nuc}}(z_0(r))}{u_\infty} \left| \frac{dr}{dz_0} \right|^{-1} \frac{S(z_0)}{S_\infty} dr, \quad (\text{S18})$$

The examples shown in Fig. S2 demonstrate that the particle size distribution sensitively depends on the parameters of the random channels.

3.3 Ensemble of random channels

In Fig. S3 the distributions of gas velocity, density, temperature and solid phase fraction at the outlet are shown for an ensemble of 5,000 random channels, for correlation length and minimal width uniformly distributed in the intervals $L_0 \in [5 \text{ m}, 40 \text{ m}]$ and $D_{\text{min}}/D_{\text{max}} \in [0.3, 0.9]$. Additionally, the distribution of R_c (see Eqs. (2, S19)), the parameter, which discriminates “fast small particles” and “slow large particles”, is shown.

In Fig. S5 we compare the size distribution of those grains that fall back to the surface to those escaping the moon and feeding the E-Ring.

3.4 Collisions of grains with the walls and interaction with the gas flow

Up to now we have implicitly assumed that the icy grains in the flux move at the gas speed. Random collisions with the channel walls, and more generally any change in the direction of the gas flow imposed by the walls, decelerates the grains relative to the gas, which subsequently are re-accelerated by gas friction. Similarly as for the particles’ growth, the interaction between the grains and the gas is described by gas-kinetic theory. This yields the equation of motion for a grain in the gas:

$$M \frac{du_{\text{grain}}}{dt} = b\pi R^2 \rho_{\text{gas}} \langle w_{\text{g}} \rangle (u_{\text{gas}} - u_{\text{grain}}), \quad (\text{S19})$$

where u_{grain} , R and $M = (4/3)\pi R^3 \rho_{\text{grain}}$ are, respectively, the velocity, radius and mass of the grain, $b = 4/3 + (1 - \beta)\pi/6$ and the average molecular speed is $\langle w_{\text{g}} \rangle = (8k_B T_{\text{gas}}/\pi m_0)^{1/2}$, where m_0 is the mass of a water molecule. A similar equation has been derived in the literature [4] for $\beta = 0$.

We model collisions of the grains with channel walls as a random Poisson process, that is, we assume that the probability to collide with a wall during an infinitesimal time interval dt is dt/τ , where τ is the average time between successive collisions with the walls. It is more convenient, however, to deal with the characteristic collision length, which we define as $L_{\text{coll}} = u_{\text{gas}}\tau$. Then, $\exp[-t/(L_{\text{coll}}/u_{\text{gas}})]$ gives the probability that no collision has occurred during a time interval $(0, t)$. Furthermore, we assume that the wall collisions are completely dissipative[†], so that the velocity of a grain is reduced to zero in a collision. Between the wall collisions the particle dynamics is governed by Eq. (S19). Therefore the velocity of a grain at the outlet is determined by the time interval between its last wall collision and the instant when the particle leaves the channel. It also follows from this equation that for a fixed grain size only the gas density, speed and temperature near the outlet, $\rho_{\text{gas}}^{\infty}$, u_{gas}^{∞} and T_{gas}^{∞} , matter for the velocity distribution.

Introducing the dimensionless grain velocity, $\hat{v} = u_{\text{grain}}/u_{\text{gas}}^{\infty}$ and time $\hat{t} = t/\tau = t u_{\text{gas}}^{\infty}/L_{\text{coll}}$ we recast the equation of motion (S19) into the form,

$$\frac{d\hat{v}}{d\hat{t}} = \left(\frac{R_c}{R}\right) (1 - \hat{v}), \quad (\text{S20})$$

where we have defined

$$R_c \equiv \frac{\rho_{\text{gas}}^{\infty}}{\rho_{\text{grain}}} \langle w_{\text{g}}^{\infty} \rangle \left[1 + \frac{\pi}{8}(1 - \beta)\right] \frac{L_{\text{coll}}}{u_{\text{gas}}^{\infty}}, \quad (\text{S21})$$

and the label "∞" denotes again values taken at the outlet. Hence, starting after a wall collision with $\hat{v}(0) = 0$ the grain will have the velocity

$$\hat{v}(\hat{t}) = 1 - \exp[-\hat{t}/(R/R_c)] \quad (\text{S22})$$

At the outlet, the contribution of particles which had the last collision in the time interval $(-\hat{t}, -\hat{t} + d\hat{t})$ is proportional to

$$e^{-\hat{t}} \hat{v} d\hat{t}, \quad (\text{S23})$$

where $e^{-\hat{t}}$ gives the probability that they haven't undergone a collision after the last. Since $d\hat{v}$ is proportional to $d\hat{t} \exp(-\hat{t} R_c/R)$, we can re-write (S23) as

$$(1 - \hat{v})^{\frac{R}{R_c} - 1} \hat{v} d\hat{v}. \quad (\text{S24})$$

The amplitude may be obtained from normalization, so the velocity distribution for grains of size R , written in terms of the dimensional variable u_{grain} reads,

$$P(u_{\text{grain}}) = \frac{R}{R_c} \left[1 + \frac{R}{R_c}\right] \frac{u_{\text{grain}}}{u_{\text{gas}}^{\infty}} \left[1 - \frac{u_{\text{grain}}}{u_{\text{gas}}^{\infty}}\right]^{\frac{R}{R_c} - 1} \quad (\text{S25})$$

This distribution has the interesting property that particles with radii $R < R_c$ are strongly peaked at the gas speed while particles with $R > R_c$ have wider distribution with a maximum at velocity smaller than u_{gas}^{∞} . Moreover, for $R > R_c$ larger particles will be successively slower, which is a direct consequence of the size dependence of the friction law (S19). It is also interesting to note that for the characteristic parameters of the problem the value of R_c is on the sub-micron range (see main paper).

[†]Numerical checks with a Monte-Carlo method, reducing the post-collisional speed to a factor ξ times the pre-collisional speed, where ξ is a random number in the interval $[0, 1]$, did not show a significant difference to the analytical treatment here.

4 Thermodynamic data

The saturated density of water vapour in the temperature interval of interest follows from the ideal gas equation, $p = k_B T \rho_{\text{gas}}/m_0$, where p is the vapour pressure, ρ_{gas}/m_0 the number density of water molecules, $m_0 = 2.992 \cdot 10^{-26}$ kg is the mass of a water molecule, and $k_B = 1.38065 \cdot 10^{-23}$ J/K is the Boltzmann constant. For the saturated vapour pressure at the vapour-ice equilibrium the following empirical equation is used [5]

$$p_{\text{eq}}^{(s.g.)}(T_{\text{gas}}) = \exp \left[\left(-2663.5/T_{\text{gas}} + 12.537 \right) \ln(10) \right] \quad (\text{S26})$$

and a similar relation for the vapour-liquid water equilibrium [5]

$$p_{\text{eq}}^{(l.g.)}(T_{\text{gas}}) = 610.8 \exp \left[-5.1421 \ln(T_{\text{gas}}/273.15) - 6828.77 \left(1/T_{\text{gas}} - 1/273.15 \right) \right]. \quad (\text{S27})$$

The water triple point temperature is $T_{\text{t.p.}} = 273.16\text{K}$, which corresponds to the saturated density of vapour, $\rho_{\text{t.p.}} = 0.00485$ kg/m³ and vapour pressure, $p_{\text{t.p.}} = 611.2$ Pa.

The density of ice is taken as $\rho_{\text{grain}} = 920\text{kg/m}^3$ and the specific heat capacity of vapour $c_{v,g} = 1384.21\text{J}/(\text{kg} \cdot \text{K})$ [5]. For the specific heat of sublimation we use a constant value $H = 2.8 \cdot 10^6$ J/kg, that is, we neglect its weak temperature dependence $dH/dT = c_{v,g} - c_{\text{ice}} \sim 10^3$ J/(kg · K) for the relevant temperature interval of $\Delta T < 70\text{K}$, which leads only to small variation, $\Delta H \ll H$. For the condensation coefficient β we use the value of $\beta = 0.20$.

5 Removal of E ring background brightness in images

We use standard software (CISSCAL) provided by the Cassini ISS team [6] for the image calibration. In the images of the Enceladus plume light scattered by E ring dust contributes significantly to the overall brightness level. For a meaningful comparison to the model this contribution must be subtracted (Fig. S8).

We construct a model for the background brightness from a part of an image, excluding a sufficiently broad vertical stripe around the satellite which is aligned with the plume axis (right panel of Fig. S8). The background is obtained from a 2D-polynomial fit, which is extrapolated over the plume and satellite region. We further exclude from the fit 24 pixels from the edges of the image, as well as the 5 % brightest pixels (to get rid of stars and gamma spikes, if any). The horizontal banding is the residual of the 2Hz noise [6] after calibration.

The image geometry is obtained with the NAIF SPICE toolkit and the scales in the image are derived from fitting an ellipse to the limb of the satellite.

6 Plume image and sensitivity of model parameters

We reconstruct an image of the model plume for the same viewing geometry and wavelength from Mie theory for smooth spheres [7]. Fig. S6 compares the Cassini image and its model counterpart as it follows from our theory. A quantitative comparison in terms of profiles of equivalent depth of the plume versus distance from the satellite is shown in Fig. 3a of the main text for various values of the collision length L_{coll} and the condensation coefficient β . The dependence on further parameters is illustrated in Fig. S7. The overall brightness level is sensitive to the variation of the condensation coefficient β when $\beta < 0.15$, while for $\beta > 0.2$ the dependence is weak. The brightness depends mildly (within a factor of order unity) on the parameters of the random channel model. Finally, the dependence on the total length of the crack, L , levels off for large L .

References

- [1] Landau, L. D. & Lifshitz, E. M. *Fluid Mechanics* (Pergamon, London, 1959).
- [2] Viisanen, Y., Strey, R. & Reiss, H. Homogeneous Nucleation Rates for Water. *Journal of Chemical Physics* **99**, 4680–4692 (1993).
- [3] Shaw, R. A. & Lamb, D. Experimental Determination of the Thermal Accommodation and Condensation Coefficients of Water. *Journal of Chemical Physics* **111**, 10659–10663 (1999).
- [4] Gombosi, T. I. & Horanyi, M. Time-dependent Numerical Modeling of Dust Halo Formation at Comets. *Astrophysical Journal* **311**, 491–500 (1986).
- [5] Peeters, P., Gielis, J. J. H. & van Dongen, M. E. H. The Nucleation Behavior of Supercooled Water Vapor in Helium. *Journal of Chemical Physics* **117**, 5647–5653 (2002).
- [6] Porco, C. C. *et al.* Cassini Imaging Science: Instrument Characteristics and Anticipated Scientific Investigations at Saturn. *Space Science Reviews* **115**, 363–497 (2004).
- [7] We use Mishchenko's Mie Code. URL <http://www.gis.nasa.gov/~crmim>.

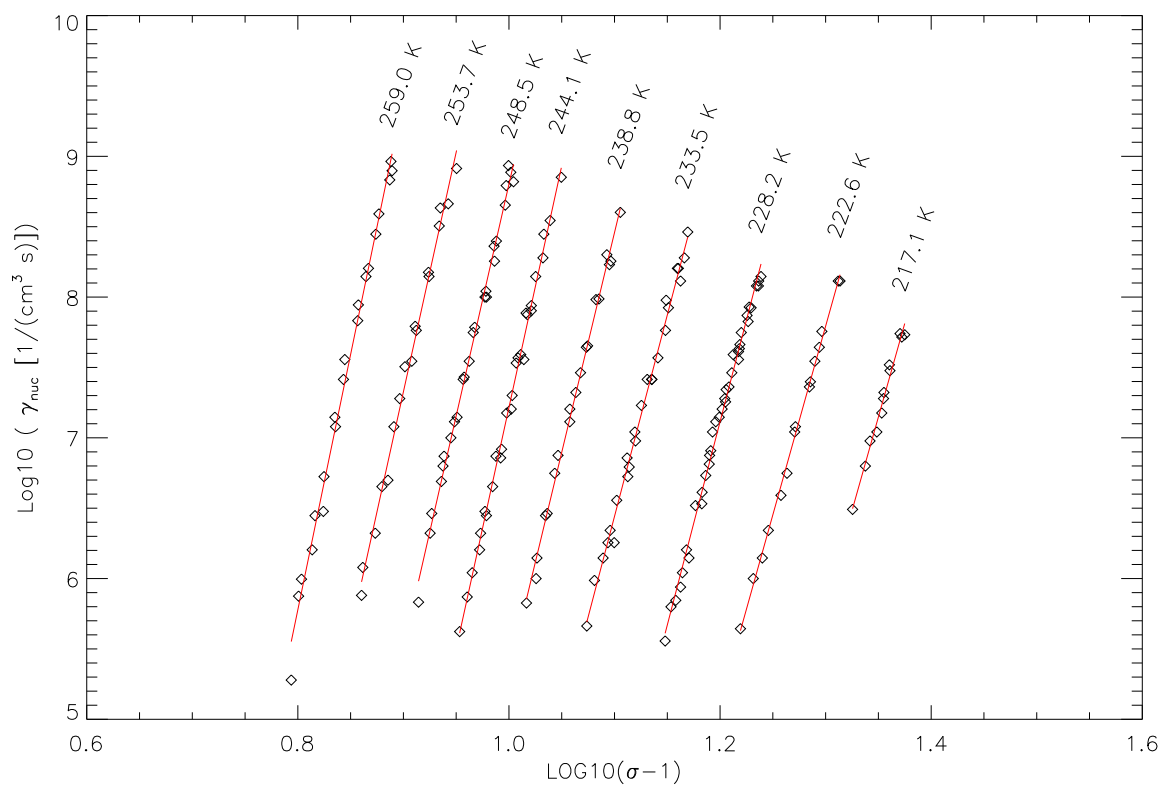


Figure S1: Nucleation rate and its dependence on super-saturation σ and temperature from experiments [2]. For fixed temperature, the data follows nicely the functional form given by Eq. (S6). We obtain the coefficients B and n for each temperature from a linear fit of $\log \gamma_{\text{nuc}}$ to $\log(\sigma - 1)$. Then $B(T)$ and $n(T)$ are obtained from quadratic fits to these coefficients (Eqs. S8, S9).

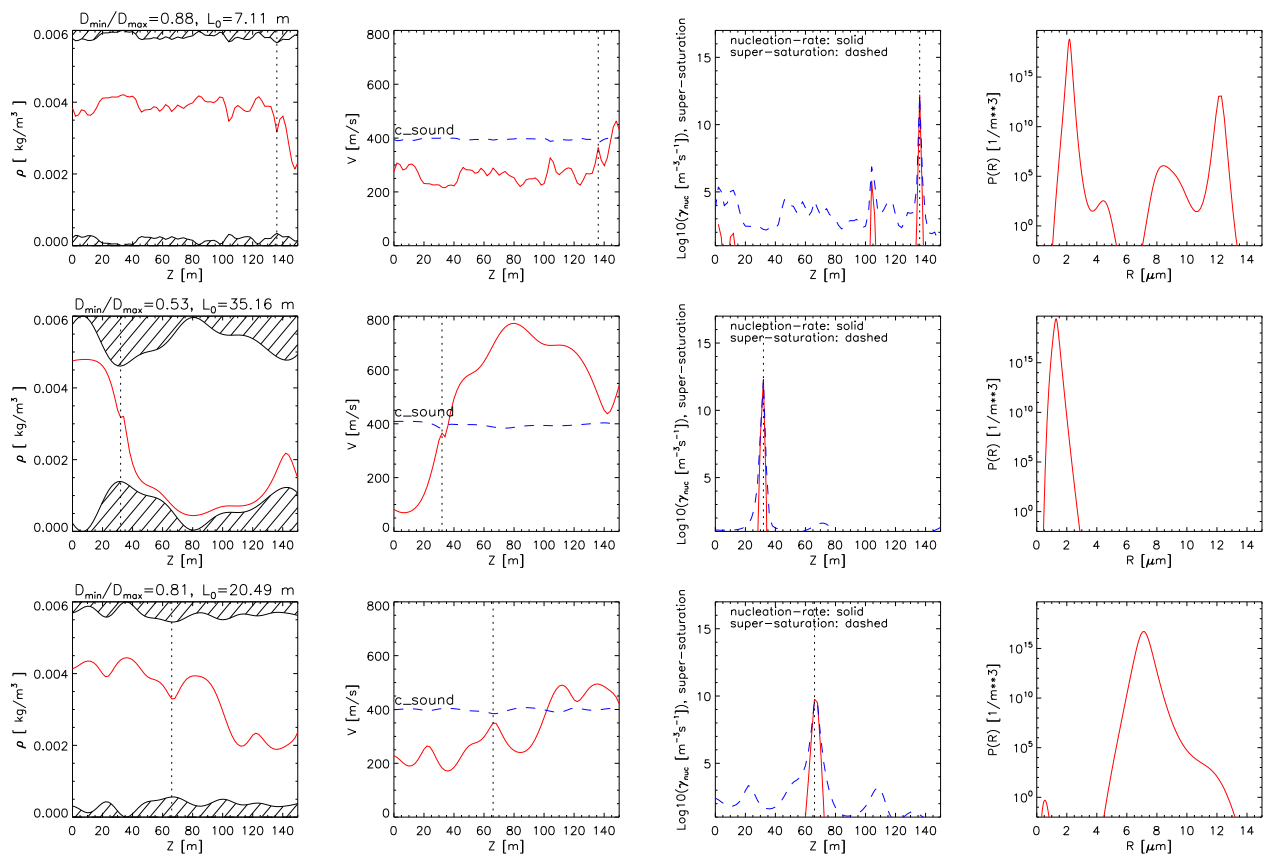


Figure S2: Examples from three runs with different random channels. From left to right: Channel profile and gas density, gas speed and speed of sound, nucleation rate and super-saturation, and particle size distribution.

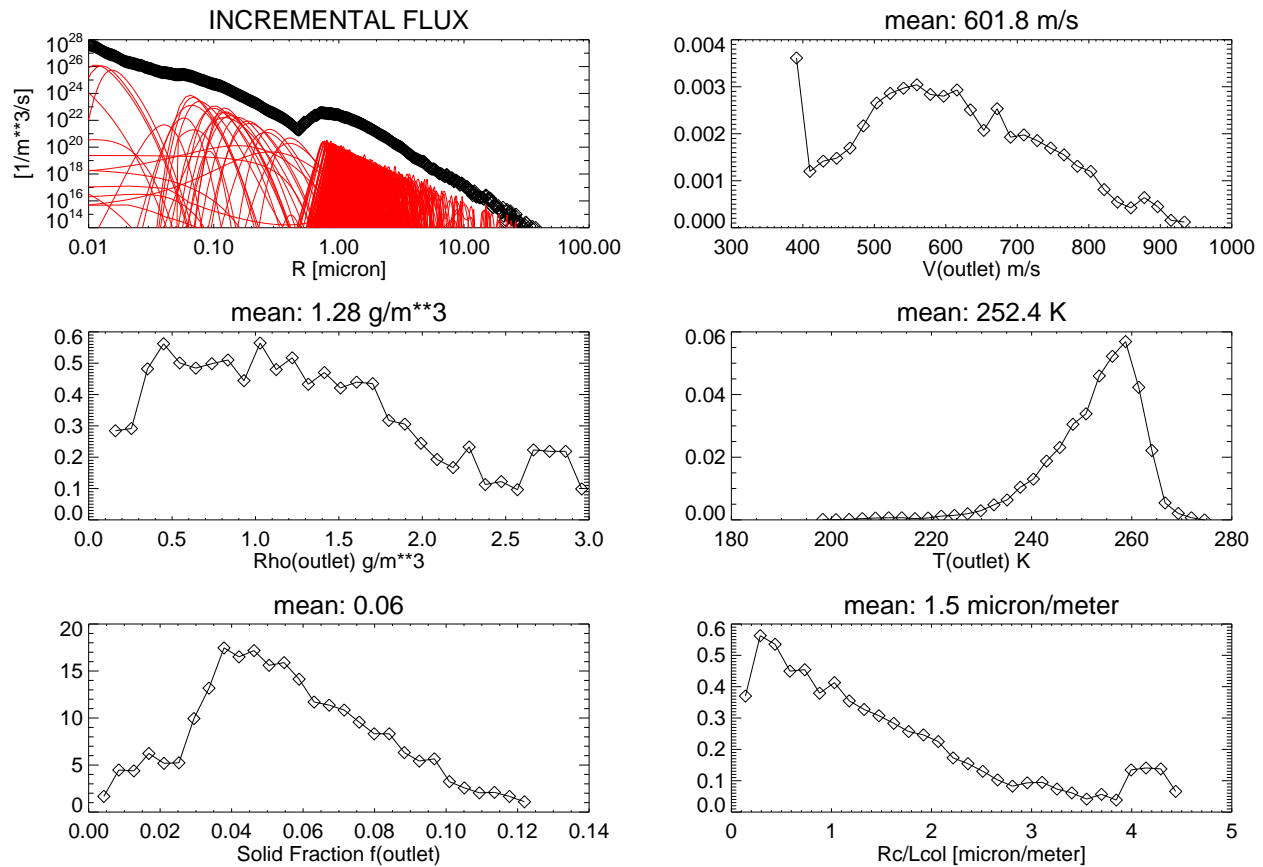


Figure S3: Results of simulations of 5,000 channels with random geometries. The total length of the channels is $L = 150$ m, the correlation length L_0 and minimal width D_{\min}/D_{\max} are uniformly distributed in the intervals, $[5 \text{ m}, 40 \text{ m}]$ and $[0.3, 0.9]$, respectively. The condensation coefficient is $\beta = 0.20$. Model variables at the channel outlet are shown (from left to right and from top to bottom): Incremental particle flux (for 500 individual runs and the sum of all 5,000), distribution of gas speed, density, temperature, fraction of the solid phase, and the critical radius R_c , separating small and large particles. From comparison to images L_{coll} is found to be on the order of ten centimetres.

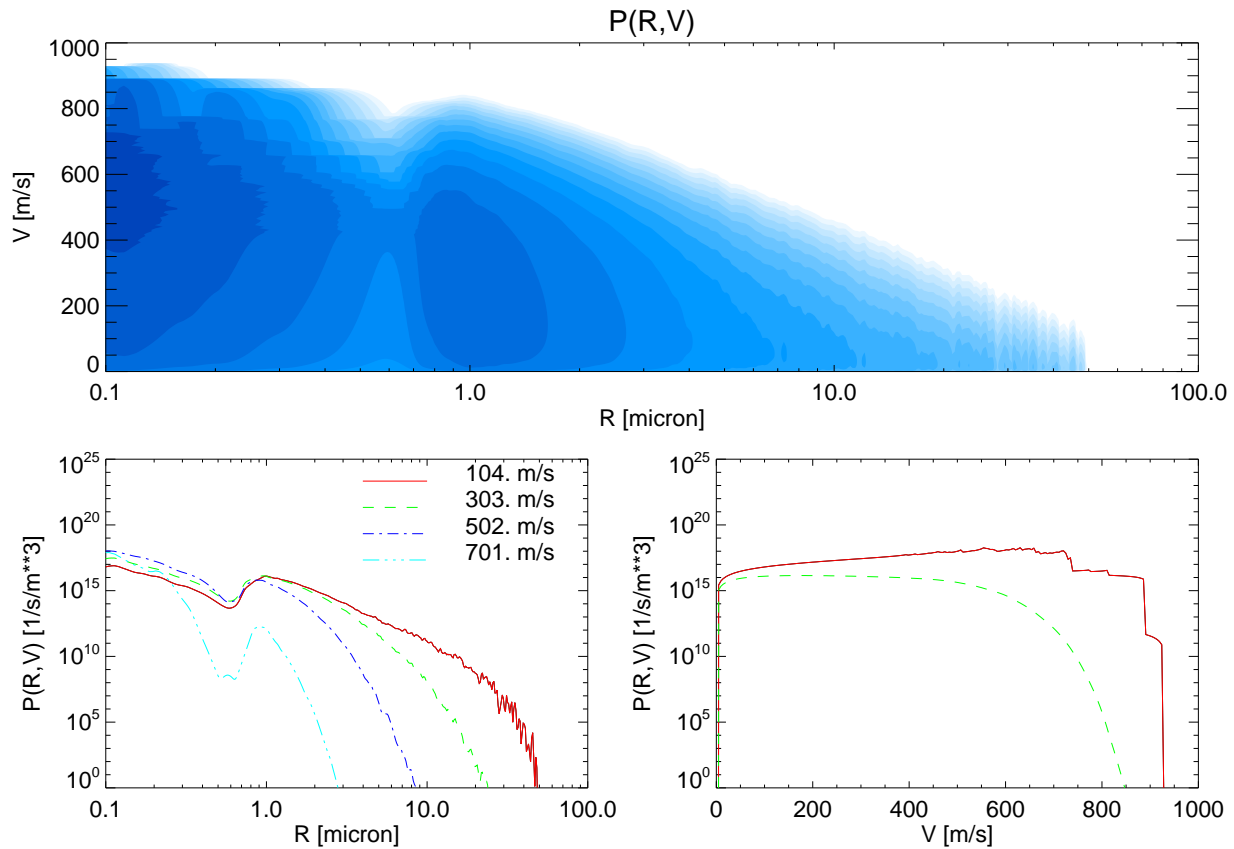


Figure S4: Speed-size-distribution for the same parameters as in Fig. S3 and $L_{\text{coll}} = 0.1$ m. Upper panel: $P(R,V)$ in log colour scale, dark colour denoting a higher number of particles. Lower panels: Cuts for various speeds (left) and grain sizes (right).

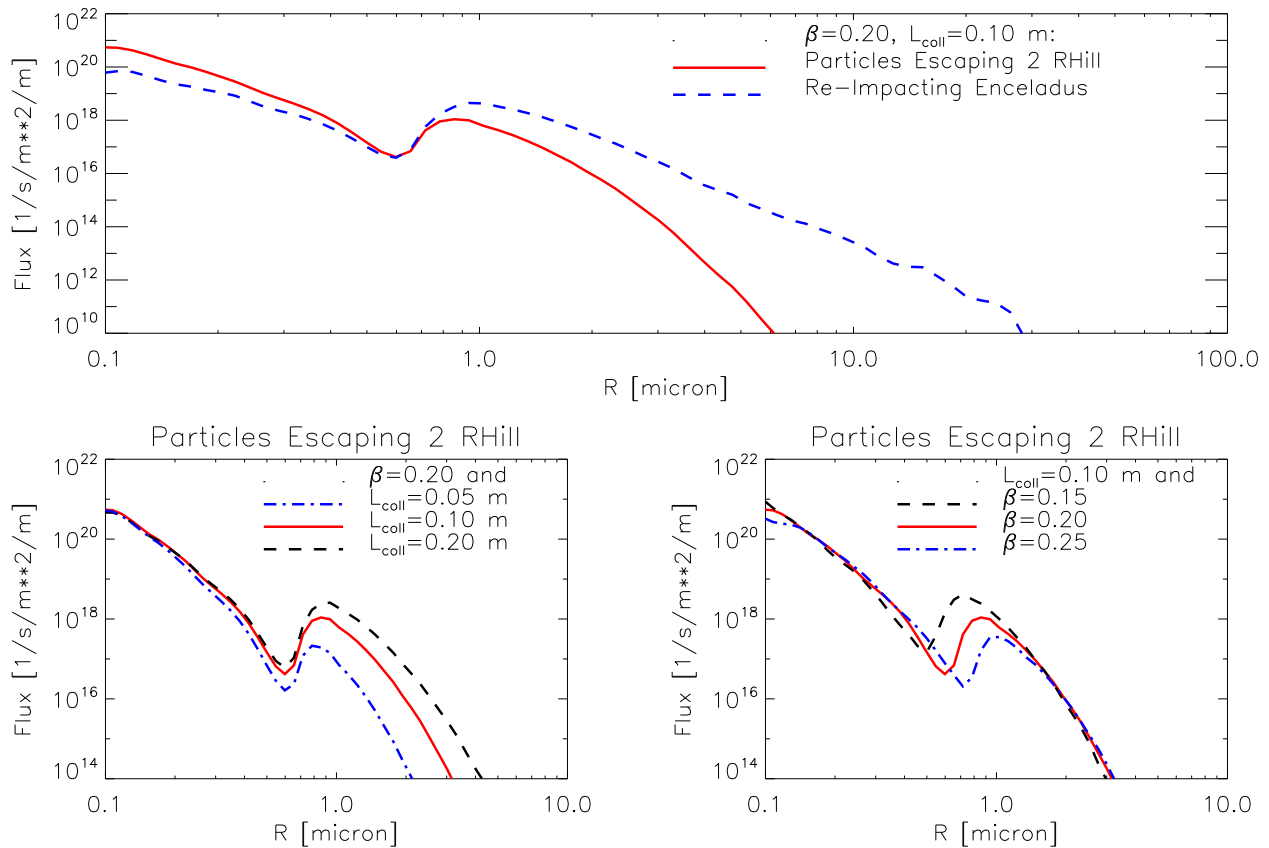


Figure S5: Upper panel: Fluxes of particles falling back to the surface (dashed) and escaping the moon (solid). The parameters are the same as in Fig. S3. Particles with the speed-size-distribution shown in Fig. S4 were launched uniformly from a circular area of 10° half-angle around the south-pole of Enceladus with starting directions uniformly distributed in a cone of 25° half-angle about the surface normal. The crossover of both distributions near 0.6 micron reflects the separation in fast and slow grains (critical radius R_c , equation (2) of the main paper). These distributions correspond to a total mass production of the dust of $30 \text{ g}/(\text{s m}^2)$ and a total mass of escaping particles of $2.5 \text{ g}/(\text{s m}^2)$. Lower panels: Effect of variation of L_{coll} (left) and β (right). The collision length L_{coll} determines the speeds for the slow grains ($R < R_c$). The condensation coefficient β shifts the local maximum of the distribution in radius and in magnitude.

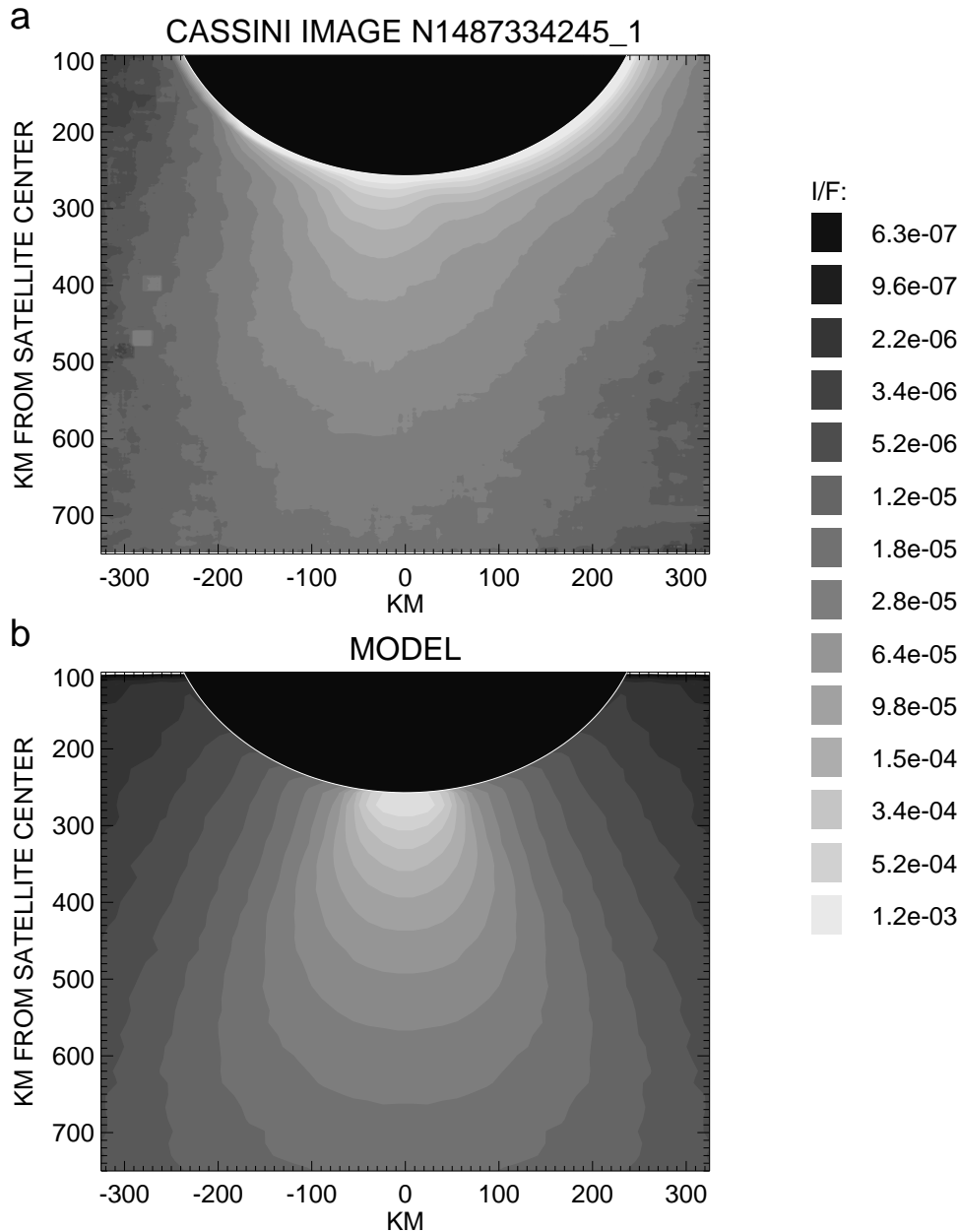


Figure S6: a) Contours of plume brightness I/F (recorded intensity I relative to solar flux πF) in the Cassini image N1487334245_1 taken on February 2005 in infrared filter (IR1, 750 nm effective wavelength) at a phase angle of 153° . The satellite is masked by a black disk. Background brightness due to E ring dust has been subtracted from the image. The enhanced brightness near the limb of the satellite, most pronounced in the right part of the image, is partly an image artefact, caused by the over-exposed sunlit surface of the moon. b) Image reconstructed from the model for the same viewing geometry and wavelength. Mie theory for smooth spheres is employed to derive the brightness. The size and spatial distributions of scattering particles follow from the plume model, discussed in the text.

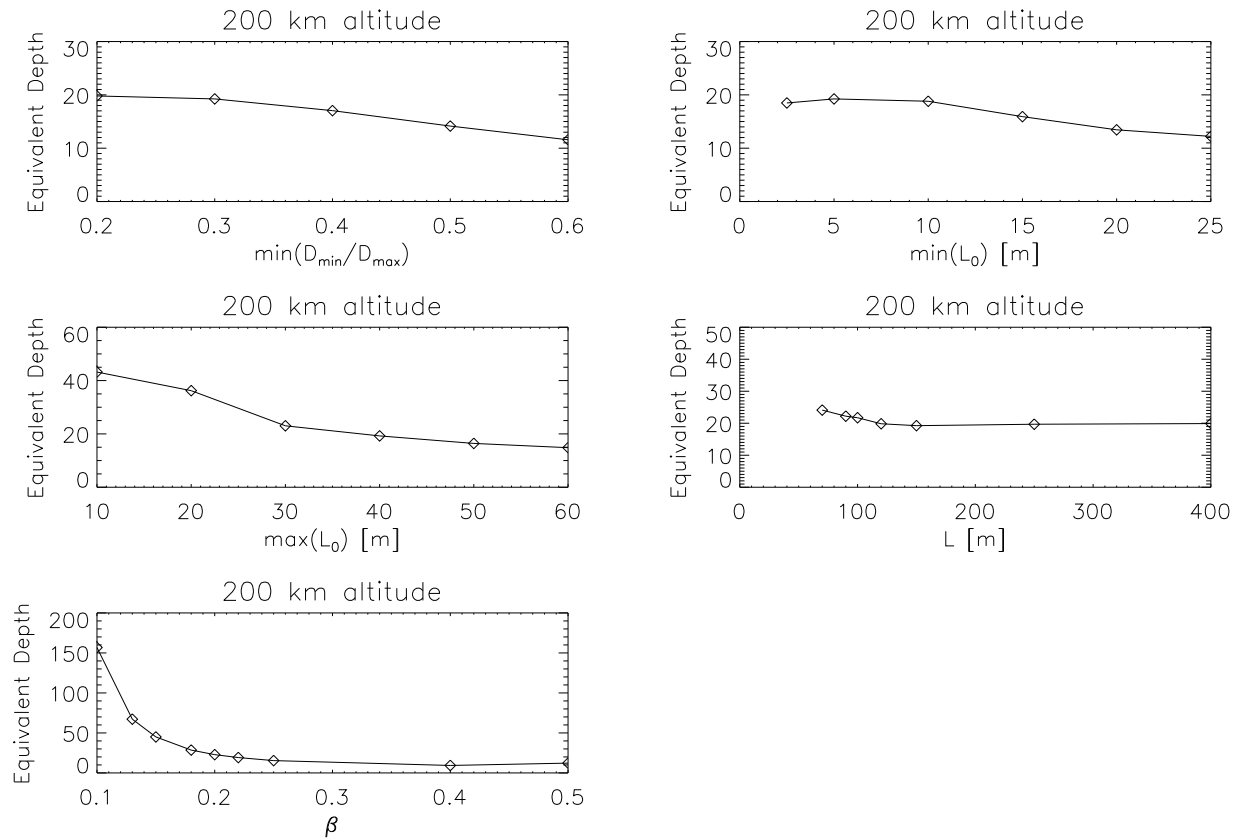


Figure S7: Variation of the equivalent depth (see caption of Fig. 3 of the main text) of the plume at an altitude of 200 km due to variation of parameters of the model. Varied are here the boundaries of the intervals from which the parameters L_0 and D_{\min}/D_{\max} are drawn, to generate the random channels, as well as the total length L and the condensation coefficient β . In each plot other parameters are fixed to $\min(D_{\min}/D_{\max}) = 0.3$, $\min(L_0) = 5$ m, $\max(L_0) = 40$ m, $L = 150$ m, and $\beta = 0.20$.

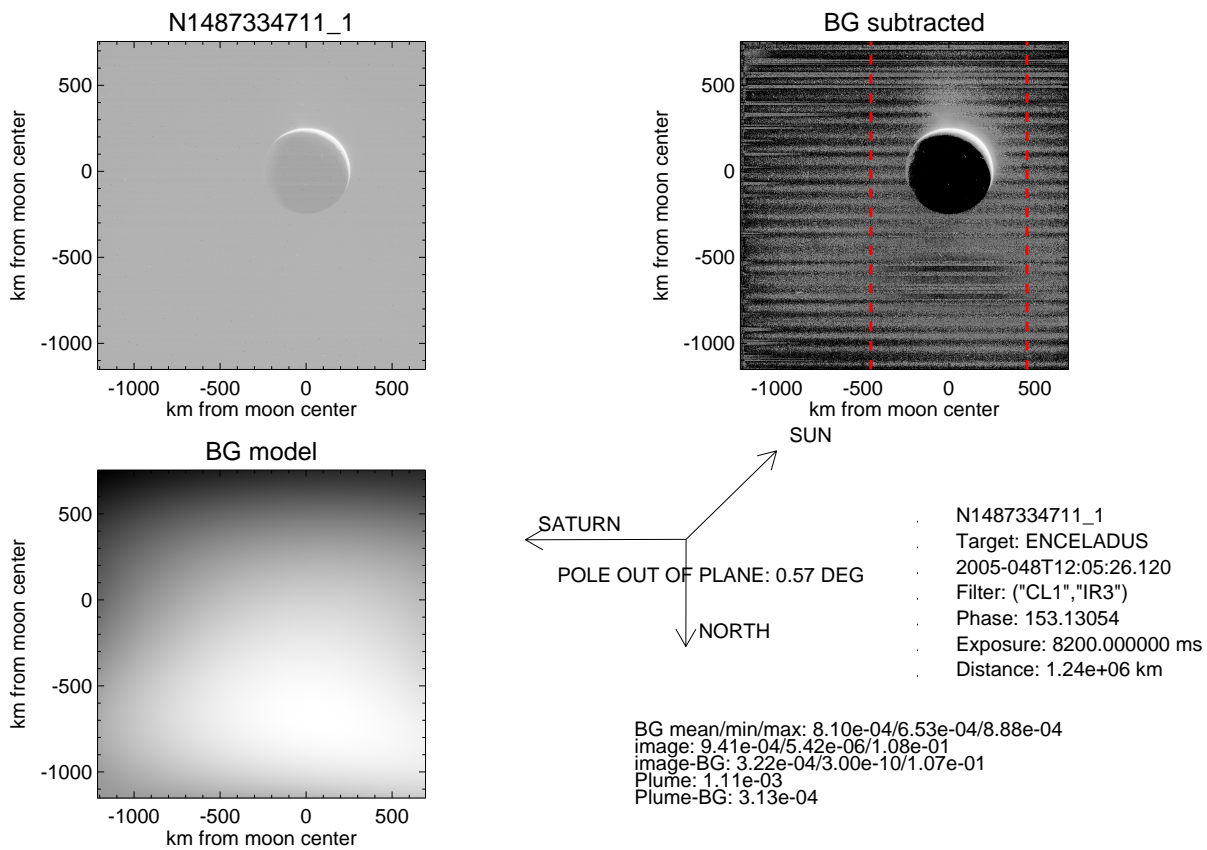


Figure S8: Decomposition into background and plume. Brightness is in log scale. The horizontal banding is the residual of the 2Hz noise [6] after calibration.